



Zn anode surface engineering for stable zinc-ion batteries: Carbon dots incorporated mesoporous TiO₂ as a coating layer

Tian-Bing Song, Qian-Li Ma, Xi-Rong Zhang, Jia-Wen Ni, Tian-Le He, Huan-Ming Xiong*

Department of Chemistry and Shanghai Key Laboratory of Molecular Catalysis and Innovative Materials, Fudan University, Shanghai 200438, PR China

ARTICLE INFO

Keywords:

Zinc ion batteries
Zinc anode
Coating layer
Carbon dots
Mesoporous TiO₂

ABSTRACT

Uncontrolled Zn dendrites growth and sustained corrosion originating from severe interfacial reactions are the major shortcomings of Zn metal electrodes in aqueous zinc-ion batteries (ZIBs). In order to overcome these obstacles, we designed a protective coating layer to stabilize the zinc anode and regulate the Zn deposition simultaneously. This hybrid layer (TiO₂/NCDs) is constructed by mesoporous TiO₂ nanosheets and N-doped carbon dots (NCDs), which is prepared by a solvothermal growth under the control of NCDs. On one hand, the TiO₂ layer immobilize water molecules effectively, preventing them from the parasitic reactions with Zn electrodes. On the other, NCDs with abundant functional groups (–OH, –COOH, –NH₂) provide the zincophilic nucleation sites to endow a small deposition overpotential of 28 mV and guide Zn deposition into a petal structure. Owing to mesoporous protective coating layer, the Zn-TiO₂/NCDs anode presents a low voltage hysteresis of 48 mV and a prolonged cycling lifespan of 1500 h at 5 mA cm⁻² and 2.5 mAh cm⁻². Moreover, aqueous ZIBs assembled with the Zn-TiO₂/NCDs anode and the α-MnO₂ cathode show outstanding reversibility and good cycling stability, whose capacity retention is up to 90% after 1000 cycles.

1. Introduction

Rechargeable aqueous batteries are regarded as green energy storage systems, because their aqueous electrolytes are much safer than those flammable organic electrolytes. Besides, aqueous electrolytes show significantly higher ionic conductivity, lower toxicity, more convenient manufacturing conditions and better cost-effectiveness than those of organic solvents [1–3]. Among the reported aqueous metal ions (Zn²⁺, Mg²⁺, Al³⁺, etc.) batteries, zinc-ion batteries (ZIBs) have received enthusiastic attention, because metallic Zn is endowed with intrinsic merits of a considerable natural abundance, a high theoretical specific capacity (820 mAh g⁻¹ or 5855 mAh cm⁻³) and a low redox potential [4,5]. Unfortunately, notorious dendrites and corrosion on the zinc surface remain major barriers against the practical ZIBs application, which always damage the cycling performance and even cause short circuit [6]. Hence, there is an imperative requirement to propose facile and effective resolutions to develop high power Zn metal batteries with long lifespans.

In the past decade, some strategies have been proposed to extend the lifespan of the Zn anode, such as constructing 3D metallic Zn structure, coating protective layers, optimizing the electrolyte composition and

redesigning separators [7–12]. Among them, surface coating is of great significance for achieving a large-scale production due to the facile preparation process. By far, the coating materials include carbons (graphene, carbon nanotube, activated carbon, carbon dots, etc.), polymers (polyamide, acrylamide, polyacrylonitrile, etc.), metals (In, Au, Ag, etc.), inorganic materials (ZrO₂, Sc₂O₃, TiO₂, CaCO₃, etc.) and various composites (metal–organic frameworks, organic–inorganic hybrids, etc.) [13–19]. Recently, TiO₂ have been widely used to protect zinc anodes due to its low cost, good electrocatalytic activity, high stability and corrosion resistance. However, TiO₂ coating layers also hinder the ion transfer at the Zn metal anode-electrolyte interface. Therefore, the improvement of the coating layer is crucial for zinc anodes. On one hand, some zincophilic layers are able to regulate the Zn nucleation sites and induce zinc ion diffusion. On the other, some hydrophobic layers are able to prevent free water molecules from corrosion on Zn electrodes, and suppress the dendrite formation. If a coating layer has both functions of the above two aspects, the Zn anode will be protected perfectly and the resulting ZIBs will work steadily for a long time.

Carbon dots (CDs), a new kind of zero-dimensional carbon nano-materials, have received wide attention and intensive research in many areas [20]. Recently, CDs have been employed in energy storage

* Corresponding author.

E-mail address: hmxiang@fudan.edu.cn (H.-M. Xiong).

<https://doi.org/10.1016/j.cej.2023.144735>

Received 31 March 2023; Received in revised form 30 June 2023; Accepted 9 July 2023

Available online 10 July 2023

1385-8947/© 2023 Elsevier B.V. All rights reserved.

systems, such as electrode components and electrolyte additives [21–23]. As for ZIBs, Ji and Hou's group firstly used CDs with $-\text{CHO}$ and $-\text{C}\equiv\text{N}$ polar groups as a functional coating layer to modify the electrolyte/Zn interfaces [24]. They proved that CDs could induce uniform Zn deposition, inhibit dendrites growth, alleviate Zn erosion and lower reactivity of water. Later, our research group synthesized nitrogen-doped and sulfonated CDs as an electrolyte additive for ZIBs [25]. Such CDs were adsorbed on the Zn anode automatically to form a protective layer, which suppressed the Zn dendrites growth and corrosion. As a result, the ZIBs showed excellent cycle life and good Coulombic efficiency. However, CDs as additives in the electrolyte could inevitably cause loss accompanied by Zn plating/stripping process during long-term cycles. And CDs in the coating layer are easy to agglomerate and weaken their surface functions.

In the present research, we used a large-scale solid phase synthesis route to prepare N-doped CDs and employed them to control the solvothermal growth of mesoporous TiO_2 . After calcination, the obtained flower-like TiO_2/NCDs hybrids were coated on Zn surface with a binder sodium alginate (SA). In this way, the Zn- TiO_2/NCDs anode was assembled into the symmetric cells, which could work for more than 3500 h at 0.5 mA cm^{-2} and 0.25 mAh cm^{-2} . Even at a higher current density of 5 mA cm^{-2} and an areal capacity of 2.5 mAh cm^{-2} , the symmetric cell could still work for over 1500 h that is close to the requirement for practical applications. In addition, Zn- $\text{TiO}_2/\text{NCDs}||\text{MnO}_2$ full cells exhibited significantly improved rate and cycling performance in comparison with the control Zn|| MnO_2 battery.

2. Experimental

2.1. Preparation of NCDs

NCDs were prepared by a large-scale solid phase synthetic method. 2 g of ethylenediamine tetraacetic acid disodium (EDTA-2Na) were ground adequately and then heated using a tubular furnace. The temperature was improved to $300 \text{ }^\circ\text{C}$ with a ramp rate of $2 \text{ }^\circ\text{C min}^{-1}$ and the sample was heated at $300 \text{ }^\circ\text{C}$ for 2 h in N_2 atmosphere. After cooling down to room temperature, the obtained sepia product was dissolved in deionized water, filtered to remove insoluble component, and then freeze-dried to obtain NCDs powder.

2.2. Preparation of TiO_2/NCDs

The mesoporous TiO_2/NCDs nanostructures were prepared solvothermally followed by a thermal treatment. Firstly, 1 mL of diethylenetriamine (DETA) was added into a mixture of 10 mL of ethylene glycol and 10 mL of isopropanol, which was kept stirring for 10 min. Then, 0.5 g of $\text{TiOSO}_4 \cdot x\text{H}_2\text{SO}_4 \cdot x\text{H}_2\text{O}$ and 2 mL of deionized water were dissolved under vigorously stirring for 30 min. Afterwards, a certain amount of NCDs was dissolved in the above solution under continuous stirring for 1 h. The obtained solution was poured into a Teflon-lined stainless-steel autoclave for 12 h heating at $180 \text{ }^\circ\text{C}$. After the solvothermal reaction, the solid product was collected by centrifugation, washed with deionized water and ethanol for several times, and dried in an oven at $80 \text{ }^\circ\text{C}$. Finally, the powder was calcined at $300 \text{ }^\circ\text{C}$ for 2 h in air to obtain the final TiO_2/NCDs composite. The samples are named as $\text{TiO}_2/\text{NCDs}_0$, $\text{TiO}_2/\text{NCDs}_5$ and $\text{TiO}_2/\text{NCDs}_{10}$ respectively, according to the different amount of NCDs added (0, 5 and 10 mg).

2.3. Preparation of MnO_2

2 mL of H_2SO_4 (0.5 mol/L) and 2.5 g of $\text{MnSO}_4 \cdot \text{H}_2\text{O}$ were added in 80 mL of deionized water and stirred magnetically. Subsequently, 1.6 g of KMnO_4 was dissolved into the clear solution which was stirred for 2 h until it became a dark-brown suspension. Then the suspension was transferred into a 100 mL of Teflon-lined stainless-steel autoclave and heated at $120 \text{ }^\circ\text{C}$ for 24 h. After the reaction, the precipitant was filtered

and washed using deionized water for several times, and dried at $70 \text{ }^\circ\text{C}$ to obtain $\alpha\text{-MnO}_2$.

2.4. Preparation of Zn- TiO_2/NCDs

The TiO_2/NCDs coating layer on bare Zn anodes (Zn- TiO_2/NCDs) were fabricated via a convenient blade-coating method. Firstly, sodium alginate (SA) powder was dissolved in deionized water to form 3 wt% of SA solution as the binder. Then, the TiO_2/NCDs powder was added under vigorously stirring for 4 h to form a homogeneous slurry that consisted of TiO_2/NCDs and SA with a weight ratio of 9:1. Next, the as-prepared slurry was spread on a Zn foil (20 μm in thickness, 99.999% of purity) by a blade-coating device, and the decorated Zn foil were placed in a vacuum oven at $110 \text{ }^\circ\text{C}$ for 12 h. They are designated as Zn- $\text{TiO}_2/\text{NCDs}_0$, Zn- $\text{TiO}_2/\text{NCDs}_5$ and Zn- $\text{TiO}_2/\text{NCDs}_{10}$ respectively, according to the difference of TiO_2/NCDs . Finally, they were tailored into circular plates with a diameter of 16 mm for assembling batteries.

2.5. Characterization

The morphological and elemental analyses of NCDs, $\text{TiO}_2/\text{NCDs}_x$ and $\alpha\text{-MnO}_2$ were characterized using a field emission scanning electron microscope (SEM, Zeiss Supra 55) and a high-resolution field-emission transmission electron microscope (HRTEM, FEI Tecnai G2 F20 S-TWIN), respectively. The X-ray diffraction (XRD) patterns were carried out by a Bruker D2 Endeavor X-ray diffractometer to explore the crystal phase of all materials. The carbon content of $\text{TiO}_2/\text{NCDs}_x$ was determined by thermogravimetric analysis (TGA8000) from $25 \text{ }^\circ\text{C}$ to $1000 \text{ }^\circ\text{C}$ at a ramp rate of $10 \text{ }^\circ\text{C min}^{-1}$ in an air. The Fourier transform infrared (FT-IR, Thermo Fisher Nicolet iS10) spectra were collected from 4000 to 400 cm^{-1} . The specific surface area was carried out by the Brunauer-Emmett-Teller (BET, Auto Chem II 2920) method. The analysis of elements was performed using a high-resolution X-ray photoelectron spectroscopy (XPS, Thermo ESCALAB 250).

2.6. Electrochemical measurements

All batteries were fabricated using 2016-type coin cells, the glass fiber films as separators (Whatman GF/D) and 2 M ZnSO_4 electrolyte. Two pieces of bare Zn or Zn- $\text{TiO}_2/\text{NCDs}_x$ were assembled as the symmetric cells, which were tested at various current densities with the charging/discharging time of 0.5 h. The asymmetric half cells of Zn||Cu and Zn||Cu- TiO_2/NCDs were fabricated to test the Coulombic efficiency and nucleation overpotential, respectively. Zn|| MnO_2 full cells were also assembled using $\alpha\text{-MnO}_2$ as the working electrodes and Zn foils or Zn- $\text{TiO}_2/\text{NCDs}_x$ foils as the counter electrodes. The $\alpha\text{-MnO}_2$ electrodes were prepared by coating the slurry of $\alpha\text{-MnO}_2$, Super P and polyvinylidene fluoride with a mass ratio of 7:2:1 in N-methyl pyrrolidone. The slurry was coated on a Ti foil and dried under vacuum at $60 \text{ }^\circ\text{C}$ for 12 h, and then punched into disks with a diameter of 12 mm. Cyclic voltammetry (CV) measurements, chronoamperometry characterization (CA), Tafel plots, and electrochemical impedance spectroscopy (EIS) were carried out on a CHI 660E electrochemical workstation, respectively. The cycling performance and the rate performance of the above cells were performed by the LAND CT2001A instrument.

3. Results and discussion

Most of the synthetic methods for CDs employ solvents at present, including hydrothermal/solvothermal, electrochemical, microwave-assisted, and strong acid decomposing reactions. These methods have two obvious drawbacks. One is the complex products, which need troublesome purification steps. The other is the low production yield, because the carbon sources are highly diluted in the reaction systems and the solvents always induce many side reactions [26]. Here we use a simple pyrolysis method to prepare NCDs from solid carbon sources, and

the product only needs water dissolution and further drying. In this way, we can obtain NCDs in a large scale soon for the subsequent reactions. The TEM images of the as-synthesized NCDs demonstrate that the products are monodispersed with uniform diameters of about 2 nm (Fig. 1 a and Fig. S1a). The corresponding HRTEM image (Fig. 1 b) shows an obvious lattice fringe spacing of 0.24 nm, in accord with the (1120) planes of graphite [27]. To probe the surface states and chemical composition of NCDs, FTIR and XPS were recorded, respectively. The FTIR spectrum of NCDs confirms various functional groups in Fig. S1b. The vibration bands at around 3436, 2820 ~ 3000, 1600, 1410 and 1130 cm^{-1} correspond to the O-H/N-H, C-H, C=O/C=N, C-N and C-O groups, respectively [28,29]. As shown in Fig. S1 c, the XPS spectrum exhibits three peaks, which ascribed to C1s, N1s and O1s, suggesting that nitrogen element has been doped into CDs successfully. In Fig. S1 d, optical features of NCDs are measured by ultraviolet-visible (UV-Vis) spectroscopy and photoluminescence (PL) spectra, respectively. The UV-Vis absorption spectra exhibit two characteristic broad bands at 270 and 330 nm, which represent the electron transitions from the π (or n) orbital to the π^* orbital of the C=C and C=O bonds, respectively [30]. The PL spectra reveal a broad blue emission at around 461 nm, which is typical for CDs in literature [31].

Fig. 1 also elaborates the synthetic route and the products with different morphologies and pore sizes. Those products are named as $\text{TiO}_2/\text{NCDs}_x$, in which x represents the amount (mg) of NCDs added in the reaction. Obviously, x plays an important role in the products formation with different morphologies. The SEM images of three samples are displayed in Fig. 1 c ~ e and Fig. S2. $\text{TiO}_2/\text{NCDs}_0$ are dense spheres, $\text{TiO}_2/\text{NCDs}_5$ look like globes with flower structure on surfaces, and $\text{TiO}_2/\text{NCDs}_{10}$ have irregular structure which is composed of nanosheets. Such morphological variations lead to the different specific surface areas and pore size distribution of the products (Fig. 1f ~ h and Fig. S3a). The pore size distribution of three samples is around 2.8, 9.5 and 6.2 nm, respectively. N_2 adsorption/desorption isotherms display that $\text{TiO}_2/\text{NCDs}_5$ has the largest specific surface areas of $163.8 \text{ m}^2 \text{ g}^{-1}$, while the

specific surface areas of $\text{TiO}_2/\text{NCDs}_0$ and $\text{TiO}_2/\text{NCDs}_{10}$ are 102.5 and $124.3 \text{ m}^2 \text{ g}^{-1}$, respectively. The $\text{TiO}_2/\text{NCDs}_5$ has the largest specific surface area and a special mesoporous structure, which is conducive to shortening the ion transfer path and improving the ion adsorption capacity [32]. Moreover, XRD patterns of $\text{TiO}_2/\text{NCDs}_5$ and $\text{TiO}_2/\text{NCDs}_{10}$ in Fig. S3 b are consistent with that of $\text{TiO}_2/\text{NCDs}_0$ (PDF #21-1272), without any impurity phase.

TEM images in Fig. 2 show the intricate morphologies of the above three samples. The $\text{TiO}_2/\text{NCDs}_0$ microspheres consist of many nanoparticles and the spaces between the nanoparticles form the porous structure (Fig. 2 a and b). In contrast, both $\text{TiO}_2/\text{NCDs}_5$ (Fig. 2 c and d) and $\text{TiO}_2/\text{NCDs}_{10}$ (Fig. 2 e and f) exhibit hierarchical nanostructures, in which plenty of nanosheets on the surface of the materials are crisscrossed and stacked together. In comparison with $\text{TiO}_2/\text{NCDs}_5$, $\text{TiO}_2/\text{NCDs}_{10}$ is composed of larger sheets and thus its pore structure is different. These results confirm that the amount of NCDs in the preparation can adjust the morphology and structure of the products. HRTEM images in Fig. 2 g and Fig. S4 show the internal delicate structures of three samples, in which the lattice spacing of 0.237 nm and 0.166 nm attributed to the (004) and (211) crystal planes of TiO_2 , while the lattices spacing of 0.24 nm is owing to the typical graphite planes of NCDs. Moreover, the selected area electron diffraction (SAED) exhibits clear diffraction signals assigned to the (101), (103) and (004) planes of TiO_2 (inset of Fig. 2 g). It is clear that TiO_2 nanosheets and NCDs are combined tightly which assures the effect of NCDs on the structure and morphology of TiO_2 . In addition, the EDS mapping $\text{TiO}_2/\text{NCDs}_5$ in Fig. 2 h displays all elements (Ti, C, N and O) are evenly distributed, confirming that NCDs locate in the composite homogeneously.

In agreement with the EDS mapping, the full XPS spectra of $\text{TiO}_2/\text{NCDs}_0$ has only two peaks around 284.6 and 531.6 eV corresponded to C1s and O1s peaks, while those of $\text{TiO}_2/\text{NCDs}_5$ and $\text{TiO}_2/\text{NCDs}_{10}$ have N1s peaks at 398.2 eV (Fig. 3 a). In Fig. S5, the FTIR spectra of these samples are compared. The C-H vibration bands of NCDs are observed in $\text{TiO}_2/\text{NCDs}_x$ samples except TiO_2 , and the FTIR vibration at 1120 cm^{-1}

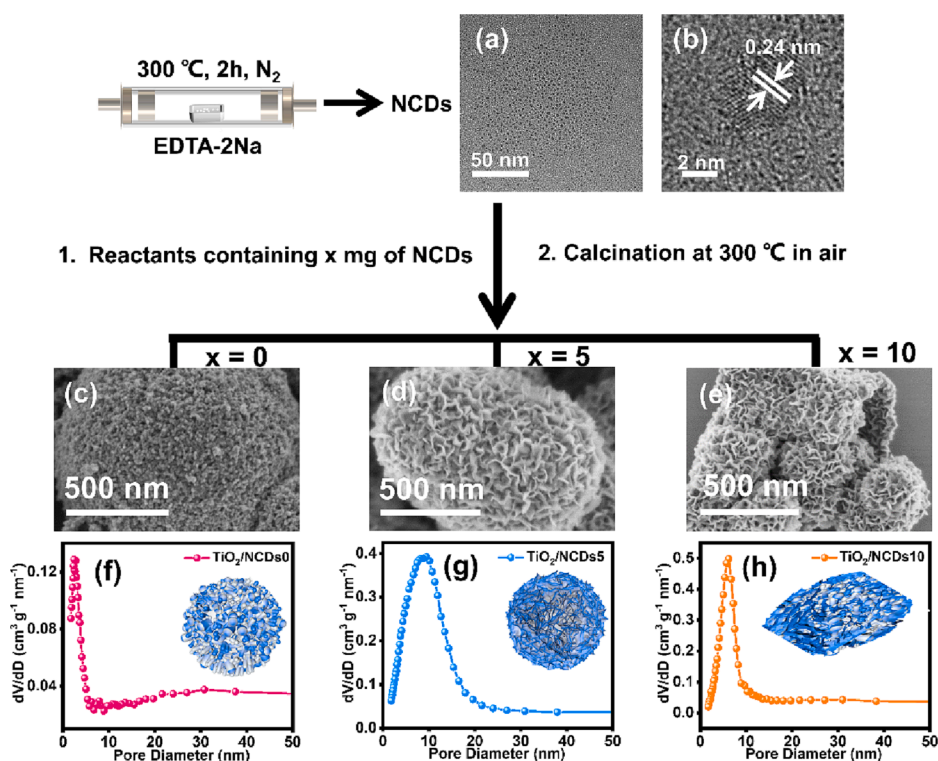


Fig. 1. The solid phase synthesis route for $\text{TiO}_2/\text{NCDs}_x$ composites with three different reactant ratios ($x = 0, 5$ and 10). (a) TEM and (b) HRTEM images of NCDs; (c ~ e) SEM images of $\text{TiO}_2/\text{NCDs}_x$; (f ~ h) pore size distributions of the above samples, with the inset schemes representing different structures and morphologies, respectively.

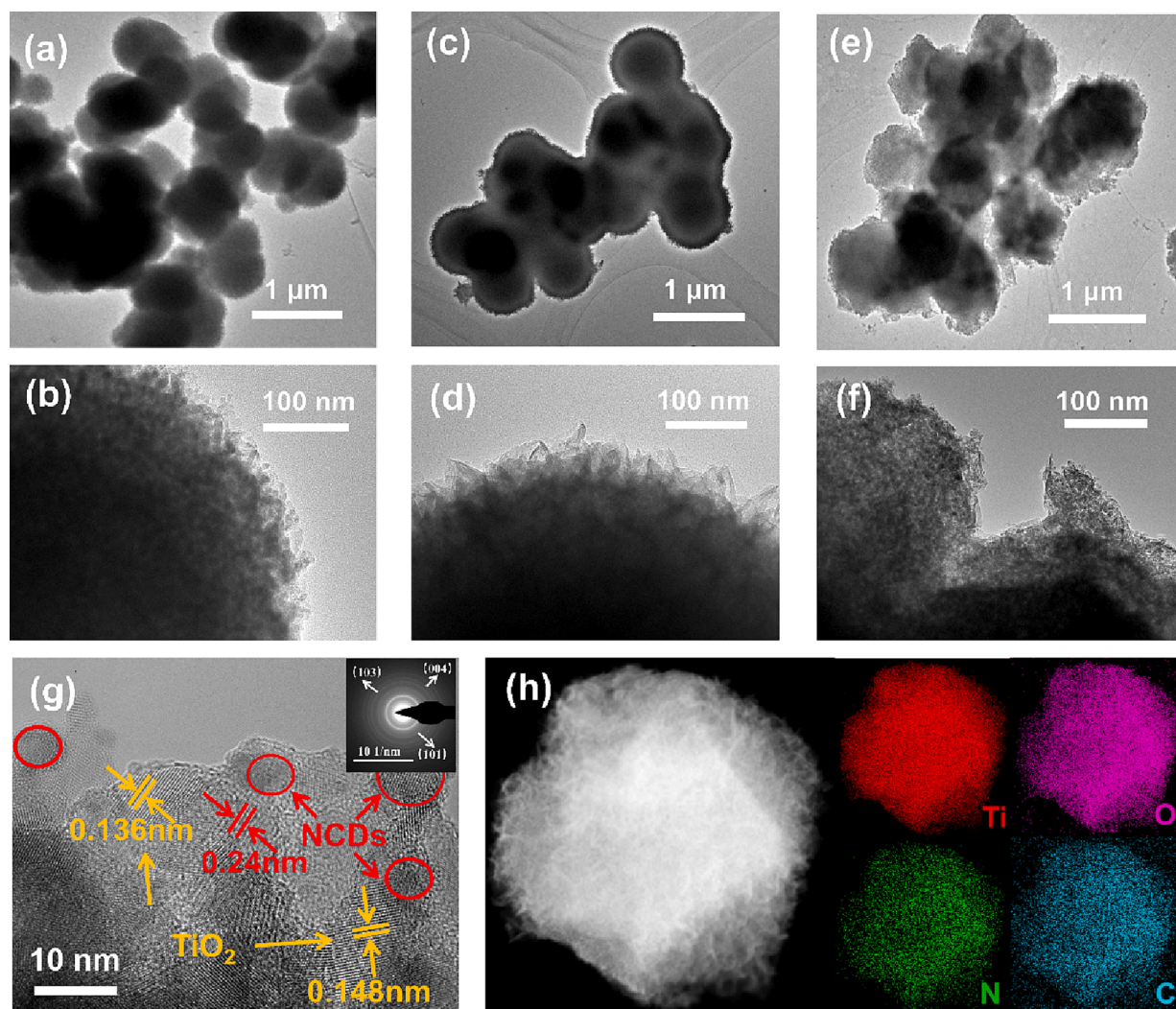


Fig. 2. TEM images of (a, b) $\text{TiO}_2/\text{NCDs}_0$, (c, d) $\text{TiO}_2/\text{NCDs}_5$ and (e, f) $\text{TiO}_2/\text{NCDs}_{10}$. (g) HRTEM image of $\text{TiO}_2/\text{NCDs}_5$ with the inset SEAD pattern. (h) EDX mapping of the same $\text{TiO}_2/\text{NCDs}_5$ sample with Ti (red), O (purple), N (green), and C (blue) elements. (For interpretation of the references to colour in this figure legend, the reader is referred to the web version of this article.)

is strengthened for both $\text{TiO}_2/\text{NCDs}_5$ and $\text{TiO}_2/\text{NCDs}_{10}$ which may be attributed to the combination between NCDs and TiO_2 . NCDs have strong blue fluorescence under UV light. In Fig. S6, both PL emission spectra and the photos under UV light confirm that $\text{TiO}_2/\text{NCDs}_{10}$ has stronger fluorescence than $\text{TiO}_2/\text{NCDs}_5$, while the $\text{TiO}_2/\text{NCDs}_0$ sample has no fluorescence. TGA analyses were carried out to evaluate the contents of NCDs in the composites, as shown in Fig. 3 b. All three samples exhibit a weight loss of ~ 5.8 wt% below 150°C , owing to the elimination of the adsorbed water. The mass loss between 150°C and 1000°C is mainly from the decomposition of residual organic species and NCDs, which are 5.6 wt%, 7.2 wt% and 9.5 wt% in different samples respectively [33]. For $\text{TiO}_2/\text{NCDs}_5$ and $\text{TiO}_2/\text{NCDs}_{10}$, the higher weight loss proves the successful incorporation of NCDs in the composites.

$\text{TiO}_2/\text{NCDs}_x$ was coated onto Zn foils to form Zn- $\text{TiO}_2/\text{NCDs}_x$ using sodium alginate (SA) as the binder which has rich carboxylic groups, good electrochemical stability and high Young's modulus [34]. Fig. 3 c compares the XRD patterns of Zn- $\text{TiO}_2/\text{NCDs}_x$, Zn and TiO_2 , which have no displacement changes and impurity peaks, implying that the TiO_2/NCDs layer has been successfully coated on Zn foils. SEM images show that the surface of the Zn plate is evenly covered by well-ordered $\text{TiO}_2/\text{NCDs}_5$ (Fig. 3 d and Fig. S7), and the EDS mapping also reflects the even distribution of Ti element on the Zn surface. The cross-section SEM images (Fig. 3 e and Fig. S8 a and b) show the thicknesses of the $\text{TiO}_2/\text{NCDs}_5$

NCDs_5 coating layer is about $8\ \mu\text{m}$. Such a thin layer can promote the wettability of the Zn foil remarkably. The contact angles measurements on the bare Zn and the Zn- $\text{TiO}_2/\text{NCDs}_x$ disclose the difference clearly (see Fig. 3 f, Fig. S8 c and d). Therefore, the tight coating layer of TiO_2/NCDs is able to improve the electrolyte-anode interfaces and enhance Zn^{2+} transport kinetics in the meantime. In addition, the $\text{TiO}_2/\text{NCDs}_5$ layer is more suitable than both $\text{TiO}_2/\text{NCDs}_0$ and $\text{TiO}_2/\text{NCDs}_{10}$, because the $\text{TiO}_2/\text{NCDs}_5$ layer has the largest contact angle and the largest pore size among the three samples.

In order to study the protective effects of $\text{TiO}_2/\text{NCDs}_x$, the stability of zinc plating/stripping is evaluated by a symmetric cell. As exhibited in Fig. 4 a and Fig. S9 at a large current density of $5\ \text{mA cm}^{-2}$ with an areal capacity of $2.5\ \text{mAh cm}^{-2}$, the symmetric cell employing bare Zn electrodes breaks down after cycling for 370 h. When Zn- $\text{TiO}_2/\text{NCDs}_0$ is employed, the symmetric cell shows an improved cycle life of 910 h, but its voltage hysteresis increases up to 150 mV. In contrast, both the Zn- $\text{TiO}_2/\text{NCDs}_5$ and the Zn- $\text{TiO}_2/\text{NCDs}_{10}$ symmetric cells display extended cycling lifespans of 1500 h with very small voltage fluctuations, implying that the Zn plating/stripping becomes more reversible under the protection of TiO_2/NCDs .

After the continuous plating/stripping, the surface morphological evolution of Zn anode was studied by SEM. In Fig. 4 b and d, many small protrusions appear promiscuously on the bare zinc plate after 50 cycles,

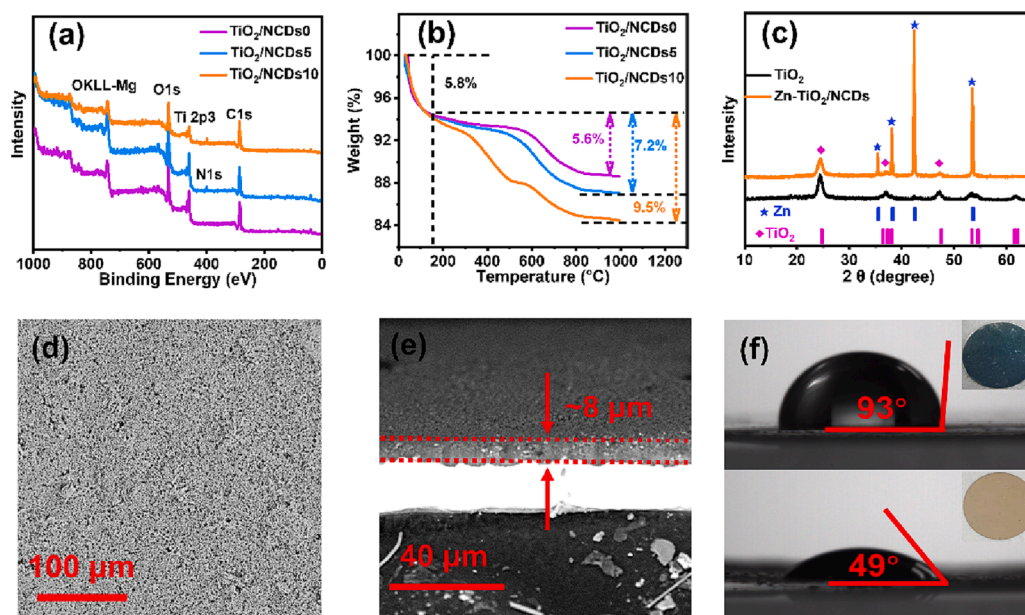


Fig. 3. (a) XPS and (b) TGA data of $\text{TiO}_2/\text{NCDs}_x$; (c) XRD patterns of TiO_2 and $\text{Zn-TiO}_2/\text{NCDs}$, respectively; (d) Plane and (e) cross-section SEM images of $\text{Zn-TiO}_2/\text{NCDs}_5$; (f) Contact angles of the electrolyte on the bare Zn (top) and the $\text{Zn-TiO}_2/\text{NCDs}_5$ (bottom) plates. The inset are the overlook photos of the corresponding samples.

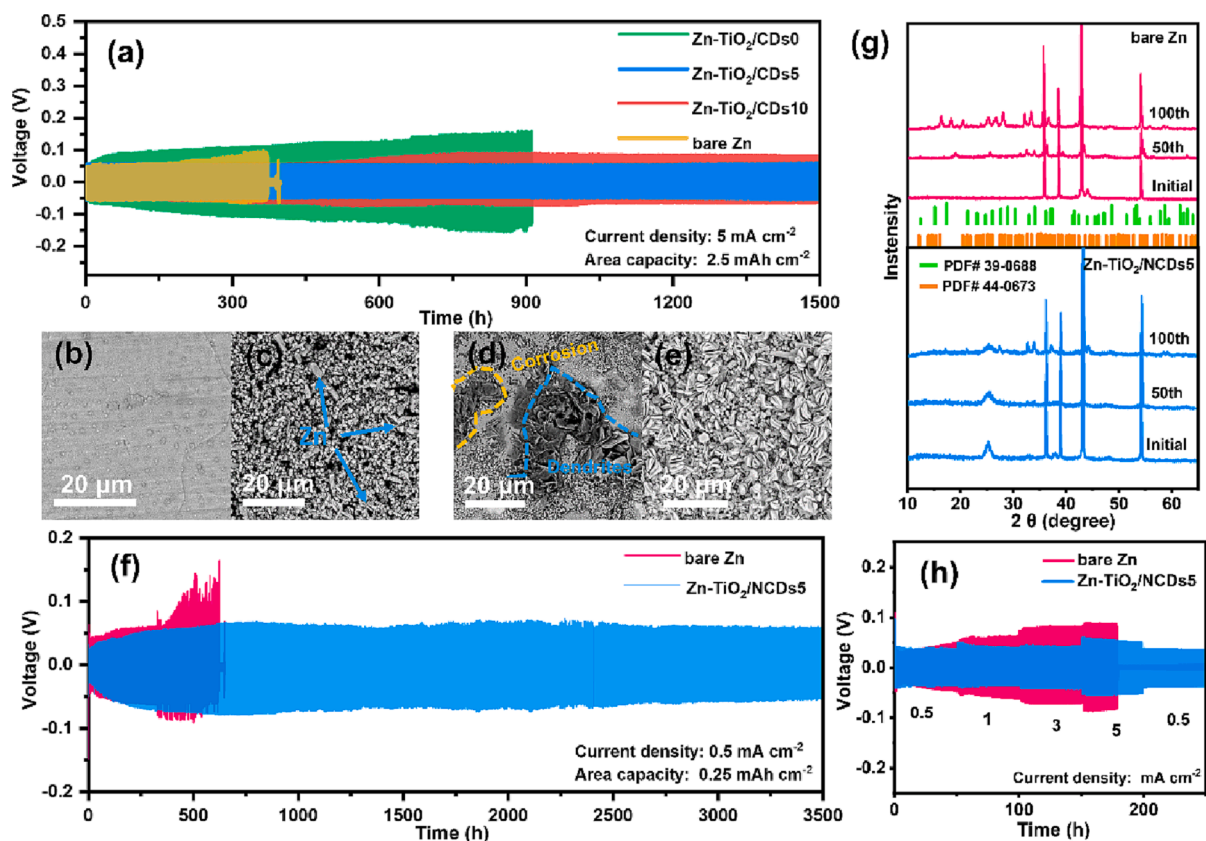


Fig. 4. (a) Cycling performance of symmetric cells at a high current density (5 mA cm^{-2}) and an areal capacity (2.5 mAh cm^{-2}); SEM images of (b, d) the bare Zn and (c, e) the $\text{Zn-TiO}_2/\text{NCDs}_5$ electrodes, (b, c) after 50 cycles and (d, e) after 200 cycles, respectively; (f) Long-term galvanostatic cycling performance, (g) XRD patterns and (h) rate performance of the bare Zn and the $\text{Zn-TiO}_2/\text{NCDs}_5$ electrodes, respectively.

and a large number of scattered flakes and corrosion pits are observed after 200 cycles. On the contrary, the $\text{Zn-TiO}_2/\text{NCDs}_5$ anode shows homogeneous Zn deposition after 50 cycles (Fig. 4 c), and the coating layer grows into small petal structures after 200 cycles (Fig. 4 e). Fig. S10

compares the SEM images of $\text{Zn-TiO}_2/\text{NCDs}_0$ and $\text{Zn-TiO}_2/\text{NCDs}_{10}$ after 200 cycles. The morphology of $\text{Zn-TiO}_2/\text{NCDs}_{10}$ is similar with that of $\text{Zn-TiO}_2/\text{NCDs}_5$, but large dendrites and protrusions in the coating layer appear on the $\text{Zn-TiO}_2/\text{NCDs}_0$. It can be inferred that NCDs are able to

provide active sites for zinc ion deposition. In addition, the abundant hydrophilic functional groups on Zn-TiO₂/NCdsx anode can immobilize water molecules around the coating layer, thereby hindering the corrosion. Tafel polarization measurements in Fig. S11 show the differences between the Zn-TiO₂/NCdsx anodes in the symmetric cells. Zn-TiO₂/NCds5 displays a lower corrosion current of 1.042 mA cm⁻² and a higher corrosion potential of -0.015 V, while the corresponding data for the bare Zn anode are 4.107 mA cm⁻² and -0.035 V respectively, which means Zn-TiO₂/NCdsx are able to protect Zn anodes against corrosion effectively [35,36].

The durability of Zn-TiO₂/NCds5 in a symmetrical cell was evaluated by the cycling performance at various current densities (Fig. 4 f and Fig. S12). The cycling performance of Zn-TiO₂/NCds5 is superior with very stable voltage profiles fluctuation. Its lifespan exceeds 3500 h and 2500 h at 0.5 mA cm⁻² and 1 mA cm⁻² respectively, which are about 6 times and 4 times higher than those data of the bare Zn electrode. After 50 cycles and 100 cycles at 0.5 mA cm⁻² and 0.25 mAh cm⁻², the cycled bare Zn and Zn-TiO₂/NCds5 electrodes were taken out for XRD measurements. In Fig. 4 g, the XRD patterns of bare Zn show the by-products of Zn₄SO₄(OH)₆·5H₂O (PDF#39-0688) and Zn₄SO₄(OH)₆·5H₂O (PDF#44-0673) grow rapidly during cycles. In contrast, the XRD results of Zn-TiO₂/NCds5 maintain the peaks of Zn and TiO₂/NCds5, and only a small number of by-products appear after 100 cycles. Hence, the TiO₂/NCds5 coating layer can effectively restrain the side reactions on Zn surface.

Under the elevated current density of 10 mA cm⁻² and areal capacity of 10 mAh cm⁻², the Zn-TiO₂/NCds5 symmetric cell maintains a reversible deposition/dissolution process without significant fluctuation within 140 h, whereas the bare Zn symmetric cell only work for 20 h (Fig. S12 b). The rate performance of symmetric cells has been cycled at the incremental current density of 0.5, 1, 3 and 5 mA cm⁻² with the areal capacity of 0.5, 1, 3 and 5 mAh cm⁻² (Fig. 4 h and Fig. S13). Zn-TiO₂/NCds5 symmetrical cell shows a much more stable voltage profile with a smaller plating/stripping over-potential (53.1 mV) even at a high current density of 5 mA cm⁻². While the current density turns back to 5 mA cm⁻², the hysteresis recovers to 35.3 mV, indicating an excellent rate reversibility of the Zn-TiO₂/NCds5. In contrast, the bare Zn anode symmetrical cell quickly fails after the current density reaches 5 mA cm⁻², demonstrating a decisive role of the TiO₂/NCds5 layer in improving cycle stability [37,38]. The cycling performance comparison between our Zn-TiO₂/NCds5 anode and those recently reported Zn anodes with various surface modification are shown in Table S1. It is clear that our Zn-TiO₂/NCds5 anode exhibits remarkable lifespans in a symmetric cell compared with the similar reports. Moreover, in order to explore the kinetics of Zn²⁺ plating/stripping, electrochemical impedance spectroscopy (EIS) was conducted in Zn symmetric cells. As illustrated in Fig. S14a, the electrode/electrolyte interfacial resistance (Rs) of Zn-TiO₂/NCds5 (1.4 Ω) is much higher than that of bare Zn (3.5 Ω) due to the hydrophilicity of the CDs layer. Notably, the Rct value of Zn-TiO₂/NCds5 anodes is much lower than bare Zn anodes suggesting fast charge transport capability, which is ascribed to the fact that abundant groups of NCDs can validly promote charge transfer and the pore structure can supply large interface areas between the electrolyte and the electrode [39,40]. To obtain better insights into the modulation of Zn stripping/plating behaviors enabled by the TiO₂/NCds5 coating, chronoamperometry (CA) and cyclic voltammetry (CV) of the cells are tested (Fig. S14 b and c). The current change of the bare Zn cell continuously increases for about 300 s in CA characterization, which indicates a long and irregular 2D diffusion mode, leading to dendrites growing on the surface. In contrast, a stable 3D diffusion process is observed in the Zn-TiO₂/NCds5 cell after a short nucleation stage of about 75 s, because the TiO₂/NCds5 coating layer induces the ordered 3D diffusion through its mesoporous structure [41,42]. The overpotential of Zn nucleation in the Zn-TiO₂/NCds5 cell is 45 mV higher than that of the bare Zn cell (Fig. S14 c), which means the stronger nucleation driving force and the smaller Zn nuclei are formed by the

TiO₂/NCds5 coating [43]. In accord with the CA analysis, the CV results confirm that the TiO₂/NCds5 coating layer can limit 2D diffusion of zinc ions, inhibit the tip effects and balance the Zn nuclei orientation growth.

Zn||Cu and Zn||Cu-TiO₂/NCds5 asymmetric cells using 2 M ZnSO₄ electrolytes are assembled to test their nucleation overpotential, Coulombic efficiency (CE) and reversibility. In Fig. 5 a, the nucleation overpotential of Zn||Cu-TiO₂/NCds5 cells is only 28 mV, much lower than that of the Zn||Cu cells (61 mV), indicating that Zn²⁺ is easier to deposit on the TiO₂/NCds5 layer [44]. And their CE are compared in Fig. 5 b. The CE of Zn||Cu-TiO₂/NCds5 cell reaches 97.0% at the 45th cycle and maintains at 98.5% even after 320 cycles, but the Zn||Cu cell only works normally within 150 cycles, and then short circuit happens with a sudden drop in CE due to severe side reactions. Moreover, the polarization voltage of the Zn||Cu cell is up to 60 mV (Fig. 5 c), while that of the Zn||Cu-TiO₂/NCds5 cell is 45 mV (Fig. 5 d). Based on the above discussed results, the comparison of the Zn plating/stripping behaviors between the bare Zn and the Zn-TiO₂/NCds5 anodes are illustrated in Scheme 1. For the bare Zn, the severe interfacial reaction with water and the uncontrolled Zn deposition results in the poor Zn plating/stripping performance (Scheme 1 a). In contrast, the TiO₂/NCds5 coating changes the situation from two aspects (Scheme 1 b). On one hand, the protective layer with hierarchical architecture immobilizes water molecules effectively, preventing them from the direct contact with Zn plate. On the other, the decorated NCDs in TiO₂/NCds5 serve as heterogeneous seeds for the even growth of Zn petals, providing favorable and abundant nucleation sites.

α-MnO₂ was synthesized hydrothermally as the cathode material [45], whose XRD patterns and SEM images are exhibited in Fig. S15. After assembly of the Zn||MnO₂ and Zn-TiO₂/NCds5||MnO₂ full cells, various electrochemical measurements are performed to compare the differences between the two cells (Fig. 6). The CV curves of both cells are similar, indicating no new electrochemical reactions are introduced by the TiO₂/NCds5 (Fig. 6a). The Zn-TiO₂/NCds5||MnO₂ cell delivers a higher peak intensity and the smaller polarization between redox peaks, reflecting the higher capacity and electrochemical reactivity than the Zn||MnO₂ cell. The rate performance of these cells is measured in Fig. 6b. At the current densities of 0.1, 0.5, 1, 2, 3 and 5 A/g, the Zn-TiO₂/NCds5||MnO₂ cell shows discharge capacities of 280.9, 252.2, 172.7, 133.3, 115.8, and 87.6 mAh g⁻¹. When the current density abruptly returns to 0.5 A/g, the capacity of Zn-TiO₂/NCds5 bounces back to 253.7 mAh g⁻¹ immediately. However, the corresponding performance of the Zn||MnO₂ cell is poor, whose capacities are lower and degrade rapidly. Notably, the initial CE of 89.3% was obtained from the Zn-TiO₂/NCds5||MnO₂ cell, higher than the cell with bare Zn anode (the initial CE of 81.1%). In Fig. 6c, the Zn-TiO₂/NCds5 delivers the higher discharge capacity of 225 mAh g⁻¹ than the bare Zn (175.8 mAh g⁻¹) and possesses the better cycling stability after 100 cycles at 0.5 A/g. The Zn-TiO₂/NCds5||MnO₂ cell even sustains a capacity retention of 89.65% after 1000 cycles at 2 A/g with a discharge capacity of 104.6 mAh g⁻¹ (Fig. 6d). The corresponding data of the Zn||MnO₂ cell are inferior obviously. The cycling performance of the Zn-TiO₂/NCds5||MnO₂ cell in our work is superior to the reported work as depicted in Table S2. Fig. S16 presents the SEM images of the deposited Zn electrodes in the Zn||MnO₂ and the Zn-TiO₂/NCds5||MnO₂ full cells after 100 cycles at 2 A/g, respectively. The former has obvious corrosion and massive sheet-like zinc dendrites, while the latter shows even zinc petals without corrosion. After 100 cycles, the EIS analyses are conducted on the two cells, which were fitted by using an equivalent circuit model (inset of Fig. 6e) to demonstrate the electrochemical processes. The resistor Rs and Rct refer to the electrolyte resistance and charge transfer resistance, respectively. The constant phase element CPE is double-layer capacitance, and the Warburg element Wo represent the ion diffusion in the host material. The Rct value of the Zn-TiO₂/NCds5||MnO₂ cell (354.4 Ω) is much smaller than Zn||MnO₂ cell (670.1 Ω), further confirming the positive effects of the TiO₂/NCds5 coating.

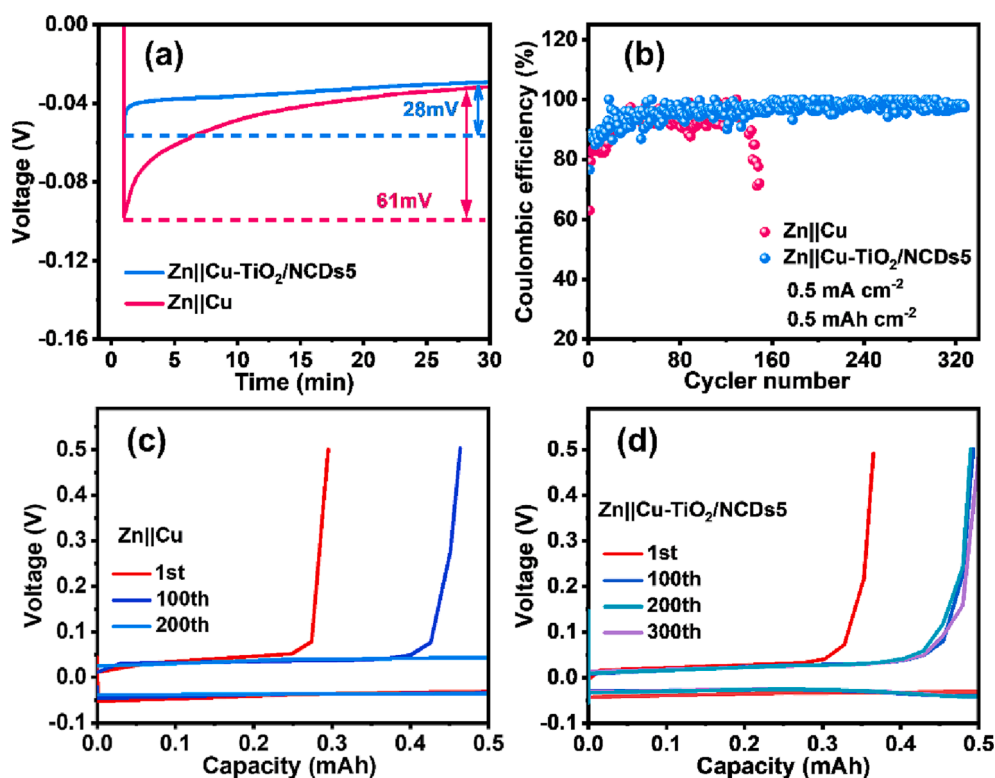
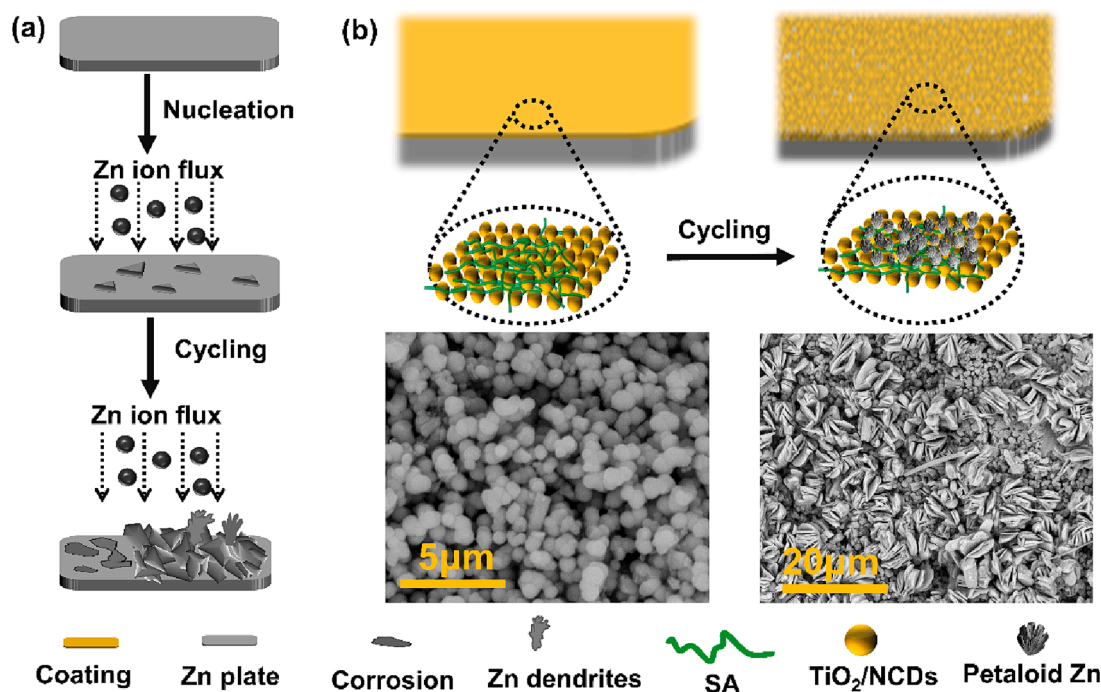


Fig. 5. (a) Nucleation overpotential and (b) Coulombic efficiency in Zn||Cu and Zn||Cu-TiO₂/NCDs5 asymmetric cells; The plating and stripping voltage profiles of (c) Zn||Cu and (d) Zn||Cu-TiO₂/NCDs5 asymmetric cells.



Scheme 1. Schematic illustrations of the Zn plating behaviors on (a) the bare Zn and (b) the Zn-TiO₂/NCDs5 electrodes, respectively.

4. Conclusion

TiO₂/NCDs composites with various morphologies are successfully synthesized through a convenient NCDs-regulated solvothermal method and a subsequent calcination treatment. Such TiO₂/NCDs are mixed with SA and coated on the Zn anode as a protective layer, in which three

components synergistically improve the electrochemical performance of the Zn-TiO₂/NCDs. Firstly, the stable and corrosion-resistant TiO₂ nanosheets form a unique structure with a high surface area of 163.8 m² g⁻¹ and a homogeneous pore size of 9.5 nm, which facilitates ion transport, suppresses dendrite growth and inhibits Zn erosion. Secondly, NCDs provide abundant active sites (-OH, -COOH, -NH₂) for Zn

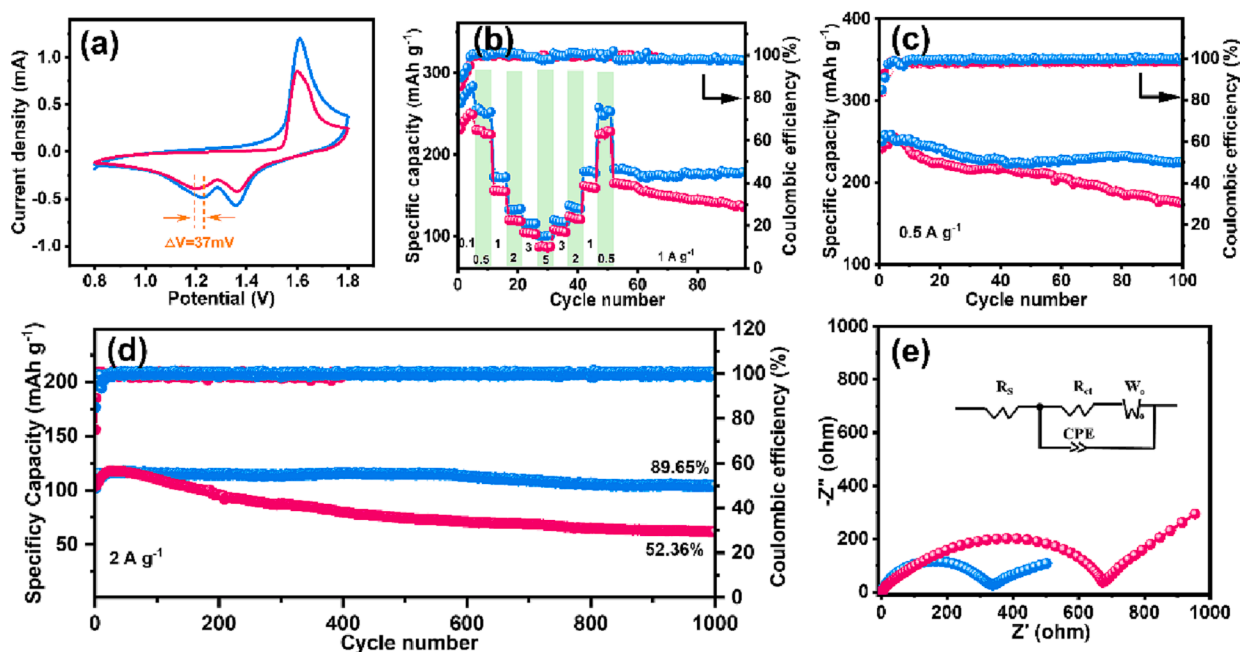


Fig. 6. Electrochemical performance of Zn||MnO₂ (red) and Zn-TiO₂/NCDs5||MnO₂ (blue) full cells: (a) cyclic voltammetry (CV) measurement at a scan rate of 0.1 mV s⁻¹, (b) rate performance, (c) cycling performance at 0.5 A/g, (d) long cycling performance at 2 A/g, and (e) EIS curves, respectively. (For interpretation of the references to colour in this figure legend, the reader is referred to the web version of this article.)

deposition and endow a small overpotential of 28 mV for the stripping/plating process, which induces the evenly electroplated Zn grow into the stable petal structure. Thirdly, SA as the binder has rich carboxylic groups, which helps TiO₂/NCDs adhere tightly on the Zn foil and improves the wettability of the whole electrode. Such a multifunctional coating layer guarantees the Zn plating/stripping with a long-term stability over 3500 h at 0.5 mA cm⁻² in the symmetric Zn-TiO₂/NCDs5||Zn-TiO₂/NCDs5 cells, and an excellent reversibility over 1000 cycles at 2 A/g in the Zn-TiO₂/NCDs5||MnO₂ full cells. Our present research confirms that the NCDs involved surface engineering on Zn anodes can greatly improve the electrochemical performance and stability of ZIBs.

Declaration of Competing Interest

The authors declare that they have no known competing financial interests or personal relationships that could have appeared to influence the work reported in this paper.

Data availability

Data will be made available on request.

Acknowledgements

This work was financially supported by the National Natural Science Foundation of China (21975048, 21771039), and the Shanghai Science and Technology Committee (19DZ2270100).

Appendix A. Supplementary data

Supplementary data to this article can be found online at <https://doi.org/10.1016/j.cej.2023.144735>.

References

- [1] Z. Yi, G. Chen, F. Hou, L. Wang, J. Liang, Strategies for the Stabilization of Zn Metal Anodes for Zn-Ion Batteries, *Adv. Energy Mater.* 11 (1) (2021) 2003065.

- [2] M. Bao, Z. Zhang, X. An, J. Liu, J. Feng, B. Xi, S. Xiong, Introducing Ce ions and oxygen defects into V₂O₅ nanoribbons for efficient aqueous zinc ion storage, *Nano Res.* 16 (2) (2023) 2445–2453.
- [3] Z. Zhang, B. Xi, X. Ma, W. Chen, J. Feng, S. Xiong, Recent progress, mechanisms, and perspectives for crystal and interface chemistry applying to the Zn metal anodes in aqueous zinc-ion batteries, *Susmat* 2 (2) (2022) 114–141.
- [4] H. Yang, Z. Chang, Y. Qiao, H. Deng, X. Mu, P. He, H. Zhou, Constructing a Super-Saturated Electrolyte Front Surface for Stable Rechargeable Aqueous Zinc Batteries, *Angew. Chemie Int. Ed.* 59 (24) (2020) 9377–9381.
- [5] Q. Zhang, J. Luan, Y. Tang, X. Ji, H. Wang, Interfacial Design of Dendrite-Free Zinc Anodes for Aqueous Zinc-Ion Batteries, *Angew. Chemie Int. Ed.* 59 (32) (2020) 13180–13191.
- [6] C. Li, X. Shi, S. Liang, X. Ma, M. Han, X. Wu, J. Zhou, Spatially homogeneous copper foam as surface dendrite-free host for zinc metal anode, *Chem. Eng. J.* 379 (2020), 122248.
- [7] B. Liu, S. Wang, Z. Wang, H. Lei, Z. Chen, W. Mai, Novel 3D Nanoporous Zn-Cu Alloy as Long-Life Anode toward High-Voltage Double Electrolyte Aqueous Zinc-Ion Batteries, *Small* 16 (22) (2020) 2001323.
- [8] L.T. Hieu, S. So, I.T. Kim, J. Hur, Zn anode with flexible β-PVDF coating for aqueous Zn-ion batteries with long cycle life, *Chem. Eng. J.* 411 (2021), 128584.
- [9] K. Zhao, G. Fan, J. Liu, F. Liu, J. Li, X. Zhou, Y. Ni, M. Yu, Y.M. Zhang, H. Su, Q. Liu, F. Cheng, Boosting the Kinetics and Stability of Zn Anodes in Aqueous Electrolytes with Supramolecular Cyclodextrin Additives, *J. Am. Chem. Soc.* 144 (25) (2022) 11129–11137.
- [10] J. Cao, D. Zhang, C. Gu, X. Zhang, M. Okhwilal, S. Wang, J. Han, J. Qin, Y. Huang, Modulating Zn deposition via ceramic-cellulose separator with interfacial polarization effect for durable zinc anode, *Nano Energy* 89 (2021), 106322.
- [11] J. Yang, H. Yan, H. Hao, Y. Song, Y. Li, Q. Liu, A. Tang, Synergetic Modulation on Solvation Structure and Electrode Interface Enables a Highly Reversible Zinc Anode for Zinc-Iron Flow Batteries, *ACS Energy Lett.* 7 (7) (2022) 2331–2339.
- [12] B. Qiu, L. Xie, G. Zhang, K. Cheng, Z. Lin, W. Liu, C. He, P. Zhang, H. Mi, Toward reversible wide-temperature Zn storage by regulating the electrolyte solvation structure via trimethyl phosphate, *Chem. Eng. J.* 449 (2022), 137843.
- [13] A. Xia, X. Pu, Y. Tao, H. Liu, Y. Wang, Graphene oxide spontaneous reduction and self-assembly on the zinc metal surface enabling a dendrite-free anode for long-life zinc rechargeable aqueous batteries, *Appl. Surf. Sci.* 481 (2019) 852–859.
- [14] X. Zeng, X. Meng, W. Jiang, M. Ling, L. Yan, C. Liang, In-situ constructing polyacrylamide interphase enables dendrite-free zinc anode in aqueous batteries, *Electrochim. Acta* 378 (2021), 138106.
- [15] X. Yang, C. Li, Z. Sun, S. Yang, Z. Shi, R. Huang, B. Liu, S. Li, Y. Wu, M. Wang, Y. Su, S. Dou, J. Sun, Interfacial Manipulation via In Situ Grown ZnSe Cultivator toward Highly Reversible Zn Metal Anodes, *Adv. Mater.* 33 (52) (2021) 2105951.
- [16] J. Cui, P. Yin, A. Xu, B. Jin, Z. Li, M. Shao, Fluorine enhanced nucleophilicity of TiO₂ nanorod arrays: A general approach for dendrite-free anodes towards high-performance metal batteries, *Nano Energy* 93 (2022), 106837.
- [17] M. Song, C. Zhong, Achieving both high reversible and stable Zn anode by a practical glucose electrolyte additive toward high-performance Zn-ion batteries, *Rare Met.* 41 (2) (2022) 356–360.

- [18] X. Luo, M. Zhou, Z. Luo, T. Shi, L. Li, X. Xie, Y. Sun, X. Cao, M. Long, S. Liang, G. Fang, Regulation of desolvation process and dense electrocrystallization behavior for stable Zn metal anode, *Energy Storage Mater.* 57 (2023) 628–638.
- [19] C.D. Díaz-Marín, L. Zhang, Z. Lu, M. Alshrah, J.C. Grossman, E.N. Wang, Kinetics of Sorption in Hygroscopic Hydrogels, *Nano Lett.* 21 (1) (2022) 119–127.
- [20] J.-S. Wei, T.-B. Song, P. Zhang, X.-Q. Niu, X.-B. Chen, H.-M. Xiong, A new generation of energy storage electrode materials constructed from carbon dots, *Mater. Chem. Front.* 4 (3) (2020) 729–749.
- [21] J.-S. Wei, T.-B. Song, P. Zhang, Z.-Y. Zhu, X.-Y. Dong, X.-Q. Niu, H.-M. Xiong, Integrating Carbon Dots with Porous Hydrogels to Produce Full Carbon Electrodes for Electric Double-Layer Capacitors, *ACS Appl. Energy Mater.* 3 (7) (2020) 6907–6914.
- [22] J.-S. Wei, Z.-Y. Zhu, X. Zhao, T.-B. Song, J.-H. Huang, Y.-X. Zhang, X. Liu, L. Chen, X.-Q. Niu, Y.-G. Wang, H.-M. Xiong, Self-assembled ZnO-carbon dots anode materials for high performance nickel-zinc alkaline batteries, *Chem. Eng. J.* 425 (2021), 130660.
- [23] W. Han, H. Lee, Y. Liu, Y. Kim, H. Chu, G. Liu, W. Yang, Toward highly reversible aqueous zinc-ion batteries: nanoscale-regulated zinc nucleation via graphene quantum dots functionalized with multiple functional groups, *Chem. Eng. J.* 452 (2023), 139090.
- [24] H. Zhang, S. Li, L. Xu, R. Momen, W. Deng, J. Hu, G. Zou, H. Hou, X. Ji, High-Yield Carbon Dots Interlayer for Ultra-Stable Zinc Batteries, *Adv. Energy Mater.* 12 (26) (2022) 2200665.
- [25] T.-B. Song, Z.-H. Huang, X.-R. Zhang, J.-W. Ni, H.-M. Xiong, Nitrogen-Doped and Sulfonated Carbon Dots as a Multifunctional Additive to Realize Highly Reversible Aqueous Zinc-Ion Batteries, *Small* 2205558 (2023).
- [26] H. Ding, X.-X. Zhou, Z.-H. Zhang, Y.-P. Zhao, J.-S. Wei, H.-M. Xiong, Large scale synthesis of full-color emissive carbon dots from a single carbon source by a solvent-free method, *Nano Res.* 15 (4) (2021) 3548–3555.
- [27] M.Y. Pudza, Z.Z. Abidin, S. Abdul-Rashid, F.M. Yassin, A.S.M. Noor, M. Abdullah, *ChemistrySelect* 4 (14) (2019) 4140–4146.
- [28] T.-B. Song, Z.-H. Huang, X.-Q. Niu, X.-R. Zhang, J.-S. Wei, H.-M. Xiong, In-Situ Growth of Mn₃O₄ Nanoparticles on Nitrogen-Doped Carbon Dots-Derived Carbon Skeleton as Cathode Materials for Aqueous Zinc Ion Batteries, *ChemSusChem* 15 (6) (2022) e202102390.
- [29] M. Moniruzzaman, J. Kim, Shape-engineered carbon quantum dots embedded on CdS-nanorods for enhanced visible light harvesting towards photocatalytic application, *Appl. Surf. Sci.* 552 (2021), 149372.
- [30] H. Ding, S.B. Yu, J.-S. Wei, H.-M. Xiong, Full-Color Light-Emitting Carbon Dots with a Surface-State-Controlled Luminescence Mechanism, *ACS Nano* 10 (1) (2016) 484–491.
- [31] J.-S. Wei, H. Ding, P. Zhang, Y.F. Song, J. Chen, Y.G. Wang, H.-M. Xiong, Carbon Dots/NiCo₂O₄ Nanocomposites with Various Morphologies for High Performance Supercapacitors, *Small* 12 (43) (2016) 5927–5934.
- [32] Y. Zhang, C. Wang, H. Hou, G. Zou, X. Ji, Nitrogen Doped/Carbon Tuning Yolk-Like TiO₂ and Its Remarkable Impact on Sodium Storage Performances, *Adv. Energy Mater.* 7 (4) (2017) 1600173.
- [33] M. Wu, Y. Gao, Y. Hu, B. Zhao, H. Zhang, Boosting sodium storage of mesoporous TiO₂ nanostructure regulated by carbon quantum dots, *Chin. Chem. Lett.* 31 (3) (2020) 897–902.
- [34] L. Ling, Y. Bai, Z. Wang, Q. Ni, G. Chen, Z. Zhou, C. Wu, Remarkable Effect of Sodium Alginate Aqueous Binder on Anatase TiO₂ as High-Performance Anode in Sodium Ion Batteries, *ACS Appl. Mater. Interfaces* 10 (6) (2018) 5560–5568.
- [35] Y. Zhang, Z. Cao, S. Liu, Z. Du, Y. Cui, J. Gu, Y. Shi, B. Li, S. Yang, Charge-Enriched Strategy Based on MXene-Based Polypyrrole Layers Toward Dendrite-Free Zinc Metal Anodes, *Adv. Energy Mater.* 12 (13) (2022) 2103979.
- [36] S. Li, J. Fu, G. Miao, S. Wang, W. Zhao, Z. Wu, Y. Zhang, X. Yang, Toward Planar and Dendrite-Free Zn Electrodepositions by Regulating Sn-Crystal Textured Surface, *Adv. Mater.* 33 (21) (2021) 2008424.
- [37] S. Wang, Q. Ran, R. Yao, H. Shi, Z. Wen, M. Zhao, X. Lang, Q. Jiang, Lamella-nanostructured eutectic zinc-aluminum alloys as reversible and dendrite-free anodes for aqueous rechargeable batteries, *Nat. Commun.* 11 (2020) 1634.
- [38] Q. Ran, S. Zeng, M. Zhu, W. Wan, H. Meng, H. Shi, Z. Wen, X. Lang, Q. Jiang, Uniformly MXene-Grafted Eutectic Aluminum-Cerium Alloys as Flexible and Reversible Anode Materials for Rechargeable Aluminum-Ion Battery, *Adv. Funct. Mater.* 33 (2023) 2211271.
- [39] H. Meng, Q. Ran, T. Dai, H. Shi, S. Zeng, Y. Zhu, Z. Wen, W. Zhang, X. Lang, W. Zheng, Q. Jiang, Surface-Alloyed Nanoporous Zinc as Reversible and Stable Anodes for High-Performance Aqueous Zinc-Ion Battery, *Nano-Micro Lett.* 14 (2022) 128.
- [40] Q. Ran, H. Shi, H. Meng, S. Zeng, W. Wan, W. Zhang, Z. Wen, X. Lang, Q. Jiang, Aluminum-copper alloy anode materials for high-energy aqueous aluminum batteries, *Nat. Commun.* 13 (2022) 576.
- [41] Z. Zhao, J. Zhao, Z. Hu, J. Li, J. Li, Y. Zhang, C. Wang, G. Cui, Long-life and deeply rechargeable aqueous Zn anodes enabled by a multifunctional brightener-inspired interphase, *Energ. Environ. Sci.* 12 (6) (2019) 1938–1949.
- [42] X. Zhou, P. Cao, A. Wei, A. Zou, H. Ye, W. Liu, J. Tang, J. Yang, Driving the interfacial ion-transfer kinetics by mesoporous TiO₂ spheres for high-performance aqueous Zn-ion batteries, *ACS Appl. Mater. Interfaces* 13 (7) (2021) 8181–8190.
- [43] Q. Lu, C. Liu, Y. Du, X. Wang, L. Ding, A. Omar, D. Mikhailova, Uniform Zn deposition achieved by Ag coating for improved aqueous zinc-ion batteries, *ACS Appl. Mater. Interfaces* 13 (14) (2021) 16869–16875.
- [44] Q. Jian, Z. Guo, L. Zhang, M. Wu, T. Zhao, A hierarchical porous tin host for dendrite-free, highly reversible zinc anodes, *Chem. Eng. J.* 425 (2021), 130643.
- [45] H. Chen, C. Dai, F. Xiao, Q. Yang, S. Cai, M. Xu, H.J. Fan, S.J. Bao, Reunderstanding the Reaction Mechanism of Aqueous Zn-Mn Batteries with Sulfate Electrolytes: Role of the Zinc Sulfate Hydroxide, *Adv. Mater.* 34 (15) (2022) 2109092.